

Intrinsic Dipole Hall effect in tMoTe₂ moiré: magnetoelectricity and contact-free signature of topological transitions

Feng-Ren Fan,^{1,2,*} Cong Xiao,^{3,2,*} and Wang Yao^{1,2,†}

¹New Cornerstone Science Laboratory, Department of Physics, University of Hong Kong, Hong Kong, China

²HKU-UCAS Joint Institute of Theoretical and Computational Physics at Hong Kong, China

³Institute of Applied Physics and Materials Engineering, University of Macau, Taipa, Macau, China

We discover an intrinsic dipole Hall effect in a variety of magnetic insulating states at integer fillings of twisted MoTe₂ moiré superlattice, including topologically trivial and nontrivial ferro-, antiferro-, and ferri-magnetic configurations. The dipole Hall current, in linear response to in-plane electric field, generates an in-plane orbital magnetization M_{\parallel} along the field, through which an AC field can drive magnetization oscillation up to THz range. Upon the continuous topological phase transitions from trivial to quantum anomalous Hall states in both ferromagnetic and antiferromagnetic configurations, the dipole Hall current and M_{\parallel} have an abrupt sign change, enabling contact free detection of the transitions through the magnetic stray field. In configurations where the linear response is forbidden by symmetry, the dipole Hall current and M_{\parallel} appear as a crossed nonlinear response to both in-plane and out-of-plane electric fields. These magnetoelectric phenomena showcase novel functionalities of insulators from the interplay between magnetism, topology and electrical polarization.

Introduction.— In magnetic insulators, in-depth exploration of magnon transport has unveiled promising opportunities for low-power-consumption information technologies [1, 2]. As the electrical counterpart of magnon, a charge neutral elementary excitation carrying electric dipole can also transport energy, momentum, as well as electrical polarization in an insulator [3]. Such a concept has caught limited attentions until very recently in the context of ferroelectrics where the dipole excitation corresponds to certain phonon [3–9]. Notably, flow of electric dipole in directions perpendicular to its moment is detectable via the accompanied magnetic stray field [9].

Rhombohedral (R) homobilayers of transition metal dichalcogenides (TMDs) is a versatile platform that hosts ferroelectricity [10, 11], intrinsic magnetism [12], and nontrivial topology [13–16]. With inversion symmetry broken, the electron affinity difference between atoms leads to an interlayer electrical polarization having opposite signs at the MX and XM stacking configurations that are related by an interlayer sliding [Fig. 1(a)] [10, 11, 17–20]. In commensurate and marginally twisted homobilayers, switching of the polarization accompanied by sliding can be achieved by a sizable out-of-plane electric field [10, 11, 20–23], forming the basis of ferroelectric functionalities.

Twisting the homobilayers by a modest angle results in a moiré pattern where stacking registries alternate between MX and XM with few nm periodicity [Fig. 1(a)]. The stacking dependent electrical polarization then becomes an antiferroelectric background pinned by the moiré, in which doped carriers experience a hexagonal superlattice with two degenerate moiré orbitals at MX and XM regions polarized in opposite layers respectively [24, 25]. Berry phase from such layer texture of carrier manifests as an emergent magnetic field of quantized flux per moiré cell [25, 26], which underlies nontriv-

ial topology of low-energy minibands [24]. With the intrinsic ferromagnetism from Coulomb exchange between moiré orbitals [12], this system has become an exciting platform for exploring quantum anomalous Hall (QAH) effects, where both integer and fractional QAH effects were observed in twisted MoTe₂ [13–16]. Through the antiferroelectric nature of the carrier wavefunction, both the magnetism and topology can be manipulated by a modest perpendicular electric field (E_{\perp}) [12, 25]. At filling factor $\nu = -1$, i.e. one hole per moiré cell, experiment has reported a continuous topological phase transition from ferromagnetic (FM) QAH to a trivial FM, with the increase of E_{\perp} [14]. Hartree-Fock calculations further suggest the existence of an antiferromagnetic (AFM) state at $\nu = -2$, featuring a topological transition from trivial to an AFM QAH upon the increase of E_{\perp} [27–29].

Here we discover an intrinsic dipole Hall effect generally present in a variety of magnetic insulating states at integer filling factors in twisted R stack TMDs homobilayers. In the insulating bulk, a pure flow of interlayer dipole excitation of the doped carrier is generated due to the *dipole Berry curvature* in superlattice minibands. Such quantum geometric origin allows linear dipole current response to an in-plane electric field E_{\parallel} , rather than the usual field gradient. On top of the equilibrium magnetization out-of-plane, the dipole Hall current generates an in-plane orbital magnetization M_{\parallel} along E_{\parallel} . Through this magnetoelectric response, an AC electrical field can thus drive magnetization oscillations up to the terahertz range. Remarkably, upon the continuous topological quantum phase transitions tuned by E_{\perp} in both the $\nu = -1$ FM and $\nu = -2$ AFM states, the dipole Hall current and the associated M_{\parallel} have an abrupt change, enabling contact-free detection of the transitions through the magnetic stray field. In the $\nu = -1$ ferro- and a $\nu = -3$ ferri-magnetic configurations where this

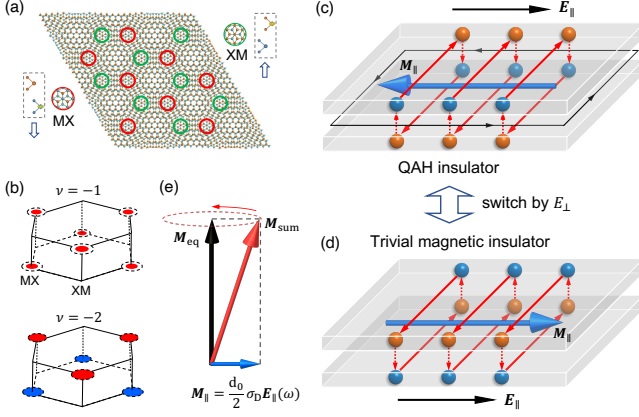


FIG. 1. (a) Schematic of twisted R-stack TMDs bilayer, featuring opposite out-of-plane electrical polarizations at MX and XM stacking regions. (b) FM and AFM insulating states at filling $\nu = -1$ and -2 . Dashed circles denote the moiré orbitals of doped carriers, polarized in opposite layers at MX and XM sites. The colored area signifies both the filling fraction and spin. (c)-(d) Dipole Hall response to in-plane electric field E_{\parallel} for (c) QAH and (d) trivial magnetic insulating state. Upon the topological phase transition controlled by perpendicular field E_{\perp} , the dipole Hall current and associated orbital magnetization M_{\parallel} (blue arrows) have an abrupt sign change. (e) Equilibrium (black) and total (red) magnetization in an AC field $E_{\parallel}(\omega)$.

linear response is forbidden at $E_{\perp} = 0$ by the $C_{2y}T$ symmetry, the dipole Hall current and M_{\parallel} appear as a non-linear response to both E_{\perp} and E_{\parallel} .

Quantum geometric origin.— For electrons in a coupled bilayer, the dipole current operator reads $\hat{j}_a = \frac{e}{2}\{\hat{v}_a, \hat{\sigma}_z\}$. Here $\hat{\sigma}_z$ is the Pauli matrix in the layer index subspace, and represents the interlayer charge dipole $\hat{\mathbf{p}} = ed_0\hat{\sigma}_z\hat{\mathbf{z}}$, where d_0 is the interlayer distance. By the semiclassical theory, the dipole current contributed by an electron is given by (see Supplemental Material [30]):

$$J_a^n(\mathbf{k}) = j_a^n(\mathbf{k}) + \Upsilon_{ab}^n(\mathbf{k})E_{\parallel,b}, \quad (1)$$

where n and \mathbf{k} are the band index and the wave vector, respectively, and summation over repeated Cartesian indices a, b is implied. The first term on the right side is the expectation value of \hat{j}_a . The second term is the *anomalous dipole current* induced by field, where

$$\Upsilon_{ab}^n(\mathbf{k}) = 2e\hbar \text{Im} \sum_{n' \neq n} \frac{j_a^{nn'}(\mathbf{k})v_b^{n'n}(\mathbf{k})}{[\varepsilon_n(\mathbf{k}) - \varepsilon_{n'}(\mathbf{k})]^2} \quad (2)$$

can be termed, in the same spirit of the spin Berry curvature [31], as *dipole Berry curvature*. Here $\varepsilon_n(\mathbf{k})$ is the band energy, and the numerator involves the interband matrix elements of interlayer-dipole current and velocity operators.

Summing over \mathbf{k} in the filled bands of the insulator yields the total dipole current density. We find

an intrinsic dipole current in linear response to E_{\parallel} : $j_{D,a} = \sigma_{ab}E_{\parallel,b}$, where $\sigma_{ab} = \sum_n \int [d\mathbf{k}] f_0(\mathbf{k}) \Upsilon_{ab}^n(\mathbf{k})$, f_0 the equilibrium Fermi distribution, and $[d\mathbf{k}]$ is shorthand for $d\mathbf{k}/(2\pi)^2$. For the off-diagonal component of dipole conductivity σ_{ab} , the threefold rotation symmetry C_{3z} forbids its symmetric part, thus $\sigma_{xy} = -\sigma_{yx}$, and the transverse transport is described by a Hall conductivity $\sigma_D = (\sigma_{xy} - \sigma_{yx})/2$. The dipole Hall current reads

$$\mathbf{j}_D = \sigma_D \mathbf{E}_{\parallel} \times \hat{\mathbf{z}}, \quad (3)$$

where the dipole Hall conductivity is given by

$$\sigma_D = \sum_n \int [d\mathbf{k}] f_0(\mathbf{k}) \Upsilon_D^n(\mathbf{k}), \quad (4)$$

with $\Upsilon_D^n(\mathbf{k}) = \epsilon_{ab} \Upsilon_{ab}^n(\mathbf{k})/2$ being the antisymmetric part of the dipole Berry curvature. Here ϵ is the Levi-Civita symbol. As a time-reversal odd pseudoscalar (zz component of a pseudotensor), σ_D is allowed by rotation and primed improper rotations (which are combinations of time reversal with inversion, mirror or roto-reflection).

Longitudinal orbital magnetoelectric response.— The interlayer-dipole Hall current is also manifested as an in-plane orbital magnetization parallel to E_{\parallel} , as shown by the schematics in Figs. 1(c) and 1(d). This is physically intuitive as a travelling charge dipole can induce an orbital magnetic moment [32]. To see this connection formally, one notices that the in-plane orbital magnetic moment operator $\hat{\mathbf{m}} = \frac{1}{4}(\hat{\mathbf{p}} \times \hat{\mathbf{v}} - \hat{\mathbf{v}} \times \hat{\mathbf{p}})$ can be recast into $\hat{\mathbf{m}} = \frac{d_0}{2} \hat{\mathbf{z}} \times \hat{\mathbf{j}}$, where $\hat{\mathbf{j}}$ is the aforementioned dipole current operator (details in [30]).

The equilibrium in-plane magnetization is prohibited by the C_{3z} symmetry. Thus, the in-plane orbital magnetization appears from the first order of electric field $M_{\parallel,a} = \chi_{ab}E_{\parallel,b}$. For the examples to be discussed, C_{3z} symmetry renders $\chi_{xx} = \chi_{yy}$, whereas M_xT symmetry forbids χ_{xy}, χ_{yx} , leaving the magnetoelectric response a longitudinal form,

$$\mathbf{M}_{\parallel} = \frac{d_0}{2} \sigma_D \mathbf{E}_{\parallel}. \quad (5)$$

Namely, this longitudinal magnetoelectric response is equivalent to the intrinsic dipole Hall effect (details in [30]). Therefore, measuring the in-plane magnetization, by magneto-optical means or via the magnetic stray field, allows a contact-free detection of the dipole Hall effect. Moreover, an AC E_{\parallel} field will drive an oscillating \mathbf{M}_{\parallel} that adds on top of the equilibrium magnetization [Fig. 1(e)], such that the net magnetization can precess with a frequency upper bounded by the charge gap, reaching THz range for the examples below.

Dipole Hall effect in the FM insulator at $\nu = -1$.— We first demonstrate the dipole Hall conductivity at $\nu = -1$ for 3.9° tMoTe₂. Figure 2(a) shows the variation of Hall conductivities with interlayer bias, from a Hartree-Fock

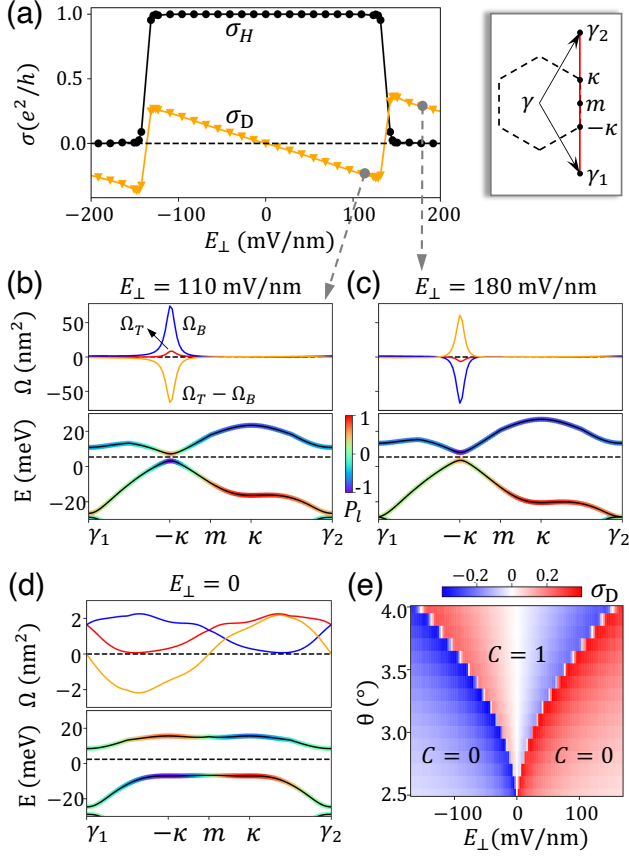


FIG. 2. Dipole Hall effect at $\nu = -1$ in tMoTe₂. (a) Charge (black circles) and dipole (orange triangles) Hall conductivity as a function of E_{\perp} . Twist angle $\theta = 3.9^{\circ}$. (b-d) Berry curvatures (upper panel) and quasiparticle band dispersion (lower panel) along k path γ_1 to γ_2 (c.f. inset for moiré Brillouin zone). The band dispersion is color coded with the layer polarization: $P_l = 1$ (-1) for Bloch states fully polarized on layer T (B). (e) Dipole Hall conductivity as a function of twist angle and E_{\perp} , where the abrupt sign changes mark the topological phase boundaries.

mean-field calculation [30]. The black-circle (orange-triangle) curve represents the charge (dipole) Hall conductivity. At small interlayer bias E_{\perp} , the FM is in a QAH state with Chern number 1, while the dipole Hall conductivity vanishes at $E_{\perp} = 0$ due to the $C_{2y}T$ symmetry. A finite E_{\perp} breaks the $C_{2y}T$ and switches on the dipole Hall effect. The FM transits from QAH to a topologically trivial state at a critical E_{\perp} , upon which the dipole Hall conductivity undergoes an abrupt change.

The simultaneous abrupt change in the charge and dipole Hall conductivities is not a coincidence. The band geometric properties arising from layer pseudospin textures underly both quantities, which become noncontinuous at the band inversion induced by the interlayer bias. To see this, we introduce layer-projected Berry curvature Ω_l ($l = T, B$) which satisfies $\Omega_T + \Omega_B = \Omega$ and $\Omega_T - \Omega_B = \Upsilon_D$, where Ω is the usual k -space Berry cur-

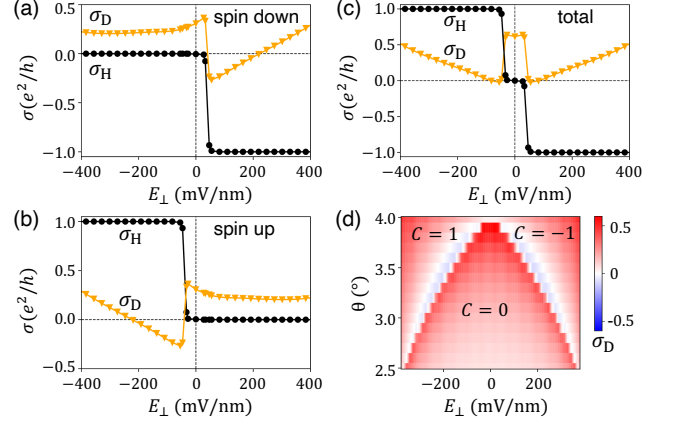


FIG. 3. Dipole Hall effect in the AFMz insulating state at $\nu = -2$ in tMoTe₂. (a)-(c) Dipole Hall (black circles) and charge Hall conductivity (orange triangles) as functions of interlayer bias for (a) spin-down, (b) spin-up, and (c) total contributions, respectively. The twist angle $\theta = 3.9^{\circ}$ (d) Dipole Hall conductivity as a function of twist angle and interlayer bias.

vature. Figures 2(b) and 2(c) show the Berry curvatures (upper panel) and band dispersion (lower panel) before and after the topological phase transition, respectively. Notably, at these positive interlayer bias, the filled band predominantly occupies layer B , and Ω_B dominates over Ω_T in magnitude. When E_{\perp} crosses the transition point, band inversion occurs in the vicinity of $-\kappa$ point, where the Berry curvatures all get reversed. As a result, an abrupt change of σ_D accompanies the change of Chern number. The reversal of the associated in-plane orbital magnetization [Figs. 1(c) and 1(d)] enables contact-free detection of this topological transition.

The phase diagram for the dipole Hall conductivity as a function of twist angle and bias is presented as Fig. 2(e). One observes that as the twist angle decreases, the critical bias for dipole-Hall jump decreases. This is because as the twist angle decreases, the energy band also narrows, and the critical bias decreases accordingly.

Dipole Hall effect in the AFM insulator at $\nu = -2$.— Compared to the case of $\nu = -1$, the $\nu = -2$ AFMz state exhibits a different symmetry, where $C_{2y}T$ is replaced by C_{2y} [Fig. 1(b)]. Therefore, a pronounced dipole Hall effect is present at $E_{\perp} = 0$ [Fig. 3(c)]. As the interlayer bias is increased, the dipole Hall conductivity undergoes a sudden jump [Fig. 3(c)] upon the topological transition to the AFMz QAH state, reminiscent of the finding in the $\nu = -1$ FM configuration. We separately examine the contributions from the spin-down and spin-up channels to charge and dipole Hall conductivities, as shown in Figs. 3(a) and (b), respectively. As the bias increases in the positive (negative) direction, the transition from trivial to QAH state occurs in the spin-down (spin-up) channel, whose contribution to the dipole Hall conduc-

tivity has a sudden sign change. The underlying picture is similar to the case of $\nu = -1$, where the band inversion in a spin channel leads to an abrupt change in both σ_D and Chern number (details in [30]).

The dependence of dipole Hall conductivity on twist angle and interlayer bias is shown in Fig. 3(d). The topological phase diagram is complementary to that of the $\nu = -1$ case, where critical E_\perp decreases with twisting angle [27]. With contributions from both spin up and down carriers, σ_D has larger magnitude here compared to the $\nu = -1$ case. Near zero interlayer bias, we find a modest $E_\parallel = 10^7$ V/m can generate a sizable in-plane orbital magnetization $M_\parallel \sim 0.01$ of μ_B/nm^2 .

Crossed nonlinear dipole Hall effect.— The study of nonlinear Hall effect is another recent focus of condensed matter physics [33–35]. With σ_D symmetry forbidden in the $\nu = -1$ state at $E_\perp = 0$, its E_\perp dependence in Fig. 2(a) implies a new type of nonlinearity — intrinsic nonlinear dipole Hall effect [Fig. 4(a)]. We can define $\Delta_D^n(\mathbf{k}) = \partial \Upsilon_D^n(\mathbf{k}) / \partial E_\perp$ as the *dipole Berry curvature polarizability* with respect to E_\perp , which is also a band geometric quantity:

$$\begin{aligned} \Delta_D^n = & \frac{e\hbar}{2} \text{Im} \sum_{m \neq n} \left[\frac{2\mathbf{j}^{nm} \times \mathbf{v}^{mn} (p^n - p^m)}{(\varepsilon_n - \varepsilon_m)^3} \right. \\ & - \sum_{\ell \neq n} \frac{(\mathbf{j}^{\ell m} \times \mathbf{v}^{mn} + \mathbf{v}^{\ell m} \times \mathbf{j}^{mn}) p^{n\ell}}{(\varepsilon_n - \varepsilon_\ell)(\varepsilon_n - \varepsilon_m)^2} \\ & \left. + \sum_{\ell \neq m} \frac{(\mathbf{j}^{\ell n} \times \mathbf{v}^{nm} + \mathbf{v}^{\ell n} \times \mathbf{j}^{nm}) p^{m\ell}}{(\varepsilon_m - \varepsilon_\ell)(\varepsilon_n - \varepsilon_m)^2} \right] \end{aligned} \quad (6)$$

and its flux through filled bands,

$$\alpha(E_\perp) = \sum_n \int [d\mathbf{k}] f_0(\mathbf{k}) \Delta_D^n(\mathbf{k}). \quad (7)$$

Substituting them into Eq. (3), we get a crossed nonlinear dipole current response,

$$\mathbf{j}_D = \alpha(0) \mathbf{E}_\parallel \times \mathbf{E}_\perp, \quad (8)$$

The concomitant nonlinear orbital magnetoelectric response is given by

$$\mathbf{M}_\parallel = \frac{d_0}{2} \alpha(0) E_\perp \mathbf{E}_\parallel. \quad (9)$$

As shown in Fig. 4(a), when the two electric fields are AC, M_\parallel have sum-frequency and difference-frequency components.

Surprisingly, Figure 2(a) shows the simple scaling of the crossed nonlinear response given in Eq. (8) and (9) is protected over the entire QAH phase, until a sudden jump occurs as the signature of the topological transition. Over such broad range of E_\perp , the variation of the minibands [Fig. 2(b,d)] does lead to significant changes

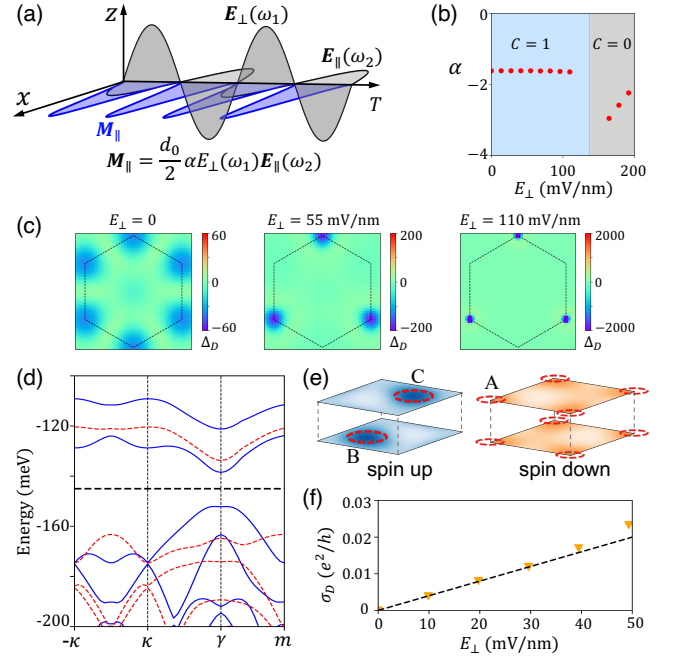


FIG. 4. Crossed nonlinear dipole Hall effect at $\nu = -1$ and -3 in tMoTe₂. (a) Schematic of the nonlinear orbital magnetoelectric response to two AC electric fields in-plane and out-of-plane. (b) The flux of dipole Berry curvature polarizability as function of E_\perp at $\nu = -1$, in unit of $\frac{nm \cdot e^2}{V \cdot h}$. (c) Distinct distributions of dipole Berry curvature polarizability in the moiré Brillouin zone at three different E_\perp in the QAH phase. (d) Quasiparticle band dispersion of $\nu = -3$ ferrimagnetic state, for which the twist angle $\theta = 3.5^\circ$. The blue-solid (red-dashed) lines represent spin-up (spin-down) bands. The black-dashed line denotes the Fermi level. (e) Layer-resolved carrier distribution of this ferrimagnetic state in a moiré supercell. Two spin-up holes occupy the B and C moiré orbitals respectively, and one spin-down hole occupies the layer-hybridized A orbital. (f) Dipole Hall conductivity as a function of interlayer bias. The black-dashed line is generated using $\sigma_D = \alpha(0)E_\perp$.

in the distribution of $\Delta_D^n(\mathbf{k})$ in the moiré Brillouin zone, as shown in Fig. 4(c). Nevertheless, their flux over the filled Chern band remains a constant in the QAH phase, in stark contrast to that in the topological trivial phases [Fig. 4(b)]. This protected scaling throughout the QAH phase is observed at other twisting angles, and also for the AFMz configuration, while the actual flux can vary modestly with angle (details in [30]).

The nonlinear dipole Hall response is not limited to QAH state. We showcase another example at filling factor $\nu = -3$, which hosts a topologically trivial ferrimagnetic insulating state, with two spin-up holes in the layer-polarized B and C orbitals and one spin-down hole in the layer-hybridized A orbital [Fig. 4(d) and 4(e)]. Details of the Hartree-Fock calculation are given in [30]. Possessing $C_{2y}T$ symmetry as well [Fig. 4(e)], the linear dipole Hall effect is forbidden at zero interlayer bias, whereas

the crossed nonlinear dipole Hall response is anticipated. This is confirmed by the calculated dipole Hall conductivity as a function of E_{\perp} given in Fig. 4(f), which shows that the response is well captured by Eq. (8) for E_{\perp} range up to 40 mV/nm.

This work is supported by the Research Grant Council of Hong Kong SAR China (AoE/P-701/20, HKU SRFS2122-7S05, A-HKU705/21) and New Cornerstone Science Foundation. C.X. acknowledges support by the UM Start-up Grant (SRG2023-00033-IAPME).

* These authors contributed equally to this work.

† wangyao@hku.hk

- [1] A. V. Chumak, V. I. Vasyuchka, A. A. Serga, and B. Hillebrands, *Nat. Phys.* **11**, 453 (2015).
- [2] H. Yu, J. Xiao, and P. Pirro, *J. Magn. Magn. Perspectives on Magnon Spintronics*, **450**, 1 (2018).
- [3] G. Bauer, P. Tang, R. Iguchi, J. Xiao, K. Shen, Z. Zhong, T. Yu, S. Rezende, J. Heremans, and K. Uchida, *Phys. Rev. Appl.* **20**, 050501 (2023).
- [4] K. Shen, *Phys. Rev. B* **106**, 104411 (2022).
- [5] L. Chotorlishvili, R. Khomeriki, A. Sukhov, S. Ruffo, and J. Berakdar, *Phys. Rev. Lett.* **111**, 117202 (2013).
- [6] G. E. W. Bauer, R. Iguchi, and K.-i. Uchida, *Phys. Rev. Lett.* **126**, 187603 (2021).
- [7] G. Chen, J. Lan, T. Min, and J. Xiao, *Chin. Phys. Lett.* **38**, 087701 (2021).
- [8] Q. Li, V. A. Stoica, M. Paściak, Y. Zhu, Y. Yuan, T. Yang, M. R. McCarter, S. Das, A. K. Yadav, S. Park, C. Dai, H. J. Lee, Y. Ahn, S. D. Marks, S. Yu, C. Kadlec, T. Sato, M. C. Hoffmann, M. Chollet, M. E. Kozina, S. Nelson, D. Zhu, D. A. Walko, A. M. Lindenberg, P. G. Evans, L.-Q. Chen, R. Ramesh, L. W. Martin, V. Gopalan, J. W. Freeland, J. Hlinka, and H. Wen, *Nature* **592**, 376 (2021).
- [9] P. Tang, R. Iguchi, K.-i. Uchida, and G. E. W. Bauer, *Phys. Rev. Lett.* **128**, 047601 (2022).
- [10] A. Weston, E. G. Castanon, V. Enaldiev, F. Ferreira, S. Bhattacharjee, S. Xu, H. Corte-León, Z. Wu, N. Clark, A. Summerfield, T. Hashimoto, Y. Gao, W. Wang, M. Hamer, H. Read, L. Fumagalli, A. V. Kretinin, S. J. Haigh, O. Kazakova, A. K. Geim, V. I. Fal'ko, and R. Gorbachev, *Nat. Nanotechnol.* **17**, 390 (2022).
- [11] X. Wang, K. Yasuda, Y. Zhang, S. Liu, K. Watanabe, T. Taniguchi, J. Hone, L. Fu, and P. Jarillo-Herrero, *Nat. Nanotechnol.* **17**, 367 (2022).
- [12] E. Anderson, F.-R. Fan, J. Cai, W. Holtzmann, T. Taniguchi, K. Watanabe, D. Xiao, W. Yao, and X. Xu, *Science* **381**, 325 (2023).
- [13] J. Cai, E. Anderson, C. Wang, X. Zhang, X. Liu, W. Holtzmann, Y. Zhang, F.-R. Fan, T. Taniguchi, K. Watanabe, Y. Ran, T. Cao, L. Fu, D. Xiao, W. Yao, and X. Xu, *Nature* **622**, 63 (2023).
- [14] H. Park, J. Cai, E. Anderson, Y. Zhang, J. Zhu, X. Liu, C. Wang, W. Holtzmann, C. Hu, Z. Liu, T. Taniguchi, K. Watanabe, J.-H. Chu, T. Cao, L. Fu, W. Yao, C.-Z. Chang, D. Cobden, D. Xiao, and X. Xu, *Nature* **622**, 74 (2023).
- [15] F. Xu, Z. Sun, T. Jia, C. Liu, C. Xu, C. Li, Y. Gu, K. Watanabe, T. Taniguchi, B. Tong, J. Jia, Z. Shi, S. Jiang, Y. Zhang, X. Liu, and T. Li, *Phys. Rev. X* **13**, 031037 (2023).
- [16] Y. Zeng, Z. Xia, K. Kang, J. Zhu, P. Knüppel, C. Vaswani, K. Watanabe, T. Taniguchi, K. F. Mak, and J. Shan, *Nature* **622**, 69 (2023).
- [17] L. Li and M. Wu, *ACS Nano* **11**, 6382 (2017).
- [18] P. Zhao, C. Xiao, and W. Yao, *npj 2D Mater. Appl.* **5**, 1 (2021).
- [19] J. Liang, D. Yang, J. Wu, J. I. Dadap, K. Watanabe, T. Taniguchi, and Z. Ye, *Phys. Rev. X* **12**, 041005 (2022).
- [20] L. Rogée, L. Wang, Y. Zhang, S. Cai, P. Wang, M. Chhowalla, W. Ji, and S. P. Lau, *Science* **376**, 973 (2022).
- [21] M. Vizner Stern, Y. Waschitz, W. Cao, I. Nevo, K. Watanabe, T. Taniguchi, E. Sela, M. Urbakh, O. Hod, and M. Ben Shalom, *Science* **372**, 1462 (2021).
- [22] C. R. Woods, P. Ares, H. Nevison-Andrews, M. J. Holwill, R. Fabregas, F. Guinea, A. K. Geim, K. S. Novoselov, N. R. Walet, and L. Fumagalli, *Nat. Commun.* **12**, 347 (2021).
- [23] K. Yasuda, X. Wang, K. Watanabe, T. Taniguchi, and P. Jarillo-Herrero, *Science* **372**, 1458 (2021).
- [24] F. Wu, T. Lovorn, E. Tutuc, I. Martin, and A. H. MacDonald, *Phys. Rev. Lett.* **122** (2019).
- [25] H. Yu, M. Chen, and W. Yao, *Natl. Sci. Rev.* **7**, 12 (2020).
- [26] D. Zhai and W. Yao, *Phys. Rev. Mater.* **4**, 094002 (2020).
- [27] F.-R. Fan, C. Xiao, and W. Yao, *Phys. Rev. B* **109**, L041403 (2024).
- [28] K. Jiang, S. Zhou, X. Dai, and Z. Wang, *Phys. Rev. Lett.* **120**, 157205 (2018).
- [29] X. Liu, C. Wang, X.-W. Zhang, T. Cao, and D. Xiao, *arXiv:2308.07488* (2023).
- [30] See Supplemental Material for the detailed derivations of Eq. (1), layer-projected Berry curvature, in-plane orbital magnetoelectric response, dipole Berry curvature polarizability, the details of Hartree-Fock mean-field method, dipole Berry curvature inversion at $\nu = -1$ and -2 , and protected scaling in the QAH phases, which includes Refs. [24, 27, 36, 37].
- [31] Y. Sun, Y. Zhang, C. Felser, and B. Yan, *Phys. Rev. Lett.* **117**, 146403 (2016).
- [32] C. Xiao and Q. Niu, *Phys. Rev. B* **104**, L241411 (2021).
- [33] Q. Ma, S.-Y. Xu, H. Shen, D. MacNeill, V. Fatemi, T.-R. Chang, A. M. Mier Valdivia, S. Wu, Z. Du, C.-H. Hsu, S. Fang, Q. D. Gibson, K. Watanabe, T. Taniguchi, R. J. Cava, E. Kaxiras, H.-Z. Lu, H. Lin, L. Fu, N. Gedik, and P. Jarillo-Herrero, *Nature* **565**, 337 (2019).
- [34] K. Kang, T. Li, E. Sohn, J. Shan, and K. F. Mak, *Nat. Mater.* **18**, 324 (2019).
- [35] Z. Z. Du, H.-Z. Lu, and X. Xie, *Nat. Rev. Phys.* **3**, 744 (2021).
- [36] C. Xiao, H. Liu, W. Wu, H. Wang, Q. Niu, and S. A. Yang, *Phys. Rev. Lett.* **129**, 086602 (2022).
- [37] C. Wang, X.-W. Zhang, X. Liu, Y. He, X. Xu, Y. Ran, T. Cao, and D. Xiao, *Phys. Rev. Lett.* **132**, 036501 (2024).